Far-field phase contrast from orbiting objects: Characterizing progenitors of binary mergers

P. Matthias[1] and R. Hofmann[2,*]

[1]*Karlsruher Institut für Technologie, Kaiserstraße 12, 76131 Karlsruhe, Germany*

[2]*Institute for Theoretical Physics, Philosophenweg 16, 69120 Heidelberg, Germany*

(Received 2 November 2017; published 29 May 2018)

We propose an idea to determine the size of a binary, composed of two compact stars or black holes, its diffractive power, the distance between components, and the distance to an observer, in exploiting the emergence of intensity contrast by free-space propagation when the phase of coherent light from a very distant background source is affected by diffraction. We assume that this effect can be characterized by the projected real part of an effective refractive index n. Here we model the according two-dimensional exit phase-map by a superposition of two Gaussians. In the extreme far field, phase information is captured by scaling functions which are analyzed here. Both spatial and temporal scanning of the intensity contrast are discussed. While the former mode can be used, e.g., to determine the distance to the observer, the latter allows, e.g., one to measure the overall diffractive power of the binary in terms of the particular dependence of a scaling curve on the projected spatial separation between the binary's components. Both modes of observation may be of relevance in monitoring the progenitor dynamics of binary collapse using radio telescopes.

DOI: 10.1103/PhysRevA.97.053845

I. INTRODUCTION

In imaging, the emergence of intensity contrast from free-space propagation of a phase-modulated, paraxial, and coherent wave field is increasingly exploited to infer properties of a three-dimensional (3D) object [1–9]. The according information is encoded in a stack of angularly displaced two-dimensional (2D) projections of the purely real refractive index n. For each exposure direction (optical axis) the corresponding projection defines the phase map $\phi(\mathbf{x}_\perp)$, where $\mathbf{x}_\perp$ denotes the vector of 2D coordinates in the object exit plane, that is, in the plane perpendicular to the optical axis immediately downstream of the object. Here, projections of the "refractive index" along parallel "lines of sight" through the object refer to respective travel-time differences of monochromatic and spatially coherent light. According to the van Cittert-Zernike theorem, the latter property is guaranteed when exploiting distant light sources [10]. Even though the electromagnetic radiation emitted by extended and strong sources, such as quasars, initially is spatiotemporally incoherent (it stems from an extended source with no phase correlations between individual atomic transitions and it exhibits a broad frequency spectrum, usually close to a black-body shape), it becomes spatially coherent upon propagation across astrophysical distances. Upon impinging on isolated stars, binaries (white dwarfs, neutron stars, black holes), or more extended objects, the wave field suffers frequency and transverse-coordinate-dependent phase shifts which are converted into intensity modulation upon further free-space propagation towards the observer. Lenseless observation within a narrow spectral bandwidth of this intensity contrast assures temporal coherence for the detected signal; for a scheme of this situation see Fig. 1. To describe the diffraction physics leading to the phase shifts, an effective refractive index or speed of propagation can be introduced, e.g., in case of a given, locally curved gravitational background space-time (gravitational lense). Here, phase shifts depend on the transversely variable effective straight-line speeds of light defined in comparison with the constant speed of light along actual geodesics.

In general, the conversion from an observed 2D map of intensity contrast to the 2D phase map—phase retrieval—represents a highly nonlocal and nonlinear problem [11]. However, under certain symmetry constraints on the phase map, such as 2D rotational or axial symmetry as well as resorting to the extreme far-field situation, exact phase retrieval often is not necessary to infer the main features of the diffracting object. Rather, essential information on the object's dimensions and diffractive power can already be extracted from the central intensity contrast's response to the variation of a length scale induced by a physical process. This is because the corresponding intensity-contrast curves are characteristic of an overall scaling of the exit phase map, defined as

$$\phi \to S\phi, \tag{1}$$

where S is a positive real number. Roughly speaking, S correlates with the overall diffractive power of the system for light emitted by a sufficiently strong, ergodic, and distant source, e.g., a quasar. That is, a reference exit phase map ϕ experiences a scaling ($S > 0$) at each spatial point $\mathbf{x}_\perp$ in the (transverse) exit plane (that is, the heights of the phase function ϕ are globally rescaled to $S\phi$), induced by a change of some physical parameter of the diffracting system, e.g., the masses of the constituent stars or black holes in a binary, leading to an associated scaling of local diffraction angles (given in terms of the gradient of $S\phi$). Since the projected distance a between the gravitational centers of the binary's constituents varies in the course of one orbit, the central intensity contrast, emergent

*r.hofmann@thphys.uni-heidelberg.de

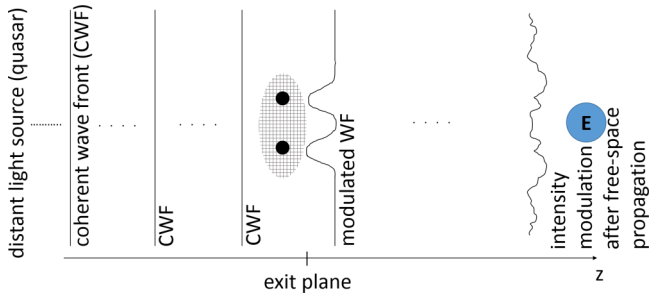

FIG. 1. Principle of the here-proposed phase-contrast modality: A distant light source of sufficient luminosity (quasar) emits electromagnetic radiation which becomes spatially coherent by propagation (defined wave fronts at given wavelength). On traversing a gravitational field (hatched area), provided by a binary system, the light waves travel along nontrivial geodesics. For each asymptotic deflection angle $\alpha \ll 1$ (constant as a function of propagation distance due to negligibility of gravitational bending outside of the interaction region) there is a contribution to the emergent wave field in the thus-defined exit plane coming from deflected and an undeflected rays. To linear order in α there is no modulation of the exit wave field's amplitude, but there is phase modulation. Upon free-space propagation to a terrestrial observer intensity (or amplitude), contrast emerges which can be analyzed without an optical system but the selection of a small spectral band.

upon free-space propagation and measured by a terrestrial observer, is a function of a. This function, however, is specific for each value of S.

The ultimate goal of the here-presented feasibility analysis is to help establish an observational modality, appealing to propagation-based phase contrast in the extreme far field, to investigate the progenitor dynamics in gravitationally bound binaries of compact stars or black holes well before their eventual merger when emitted gravitational waves become sufficiently strong to allow for terrestrial detection [12]. Note that, as of yet, there are strong observational limits in identifying and characterizing progenitors leading to supernovas and/or merging well before these events actually take place [13]. Here, we propose the observation of the spatiotemporal structure of the induced intensity contrast within radio-frequency bands as a promising venue to learn about progenitors, see again Fig. 1.

In the present work we are content with a demonstration of the principle of such a modality, and thus may assume a simplified exit phase map ϕ which is composed of a normalized superposition of Gaussians, each associated with one component of the binary, to model the deflection effects imprinted by the gravitational field. Note that for actual observations, the precise phase delays induced by an isolated star or black hole should be considered through geodesic rays. Whether the ray-optics approximation in describing the gravitationally induced phase changes is sufficient remains an open problem which we refrain from addressing.

Here, we appeal to the nonlocality expansion of the diffractogram induced by a phase map of finite support (localization), which is particularly useful in the extreme far-field limit. In this limit the lowest order of the nonlocality expansion captures the entire diffractogram with the exception of vanishing spatial frequencies [11]. Here, the term *diffractogram* refers to the 2D Fourier transform of the intensity contrast $g_z(\mathbf{x}_\perp) \equiv (I_z(\mathbf{x}_\perp) - I_0)/I_0$, taking position $\mathbf{x}_\perp$ to frequency ξ. Here, I_z denotes the intensity emergent upon free-space propagation over a distance z. I_0 is the (flat) intensity of the (parallel) and monochromatic beam (wavelength λ) impinging on the object.

By virtue of Guigay's relation [14] the nonlocality expansion orders the contribution to a diffractogram according to powers of the *overlap* of the phase map ϕ and its spatially translated version where the translation vector depends on z and ξ. Notice that such an expansion does not require S to be small [11], in contrast to various linearizations in S (and z) of the Fresnel forward problem employed for phase retrieval in the literature [1,4–8]. In the extreme far field this overlap vanishes, and the diffractogram is purely local, implying that essential information on the inducing phase map $S\phi$ already is encoded in so-called scaling functions being separated from the $\xi = (\xi_x, \xi_y)$ dependence of the diffractogram [11,15]. In the case of an astrophysical gravitational lense, which is background illuminated by a distant light source (e.g., a quasar), the spatial coherence of the impinging light can be considered perfect such that in practice there is no limit on the propagation distance z, guaranteeing the reliability of the lowest-order approximation in the nonlocality expansion.

This work is organized as follows. For readers' convenience, in Sec. II, we review the theoretical developments on the nonlocality expansion performed in [11]. In Sec. III we introduce a model for the phase map associated with the binary system. This includes a normalization which separates the effects of overall diffractive power from the influences introduced by the spatial distance between the binary's components. Explicit expressions for the intensity contrast in the far field and the extreme far field, both in 2D Fourier and position space, are given in Sec. IV. Here, the concept of scaling functions is seen to emerge. In Sec. V we discuss whether and to what extent binaries composed of two white dwarfs may give rise to observable signatures depending on their distance to the observer and the wavelength regime employed for the observation. Thereby, we distinguish two extreme cases: an observer at rest w.r.t. to the center of mass of the binary (temporal scan) and an observer who moves so fast that the internal motion of the binary can be considered frozen for the spatial distances, covered by the observer, being comparable the extent of g_z's support (spatial scan). Section VI summarizes our results, points out the potentially important role of radio-frequency observation, and the possibility of combining the here-proposed phase-contrast modality with gravitational wave observation to acquire a more complete characterization of the precollapse dynamics of binaries. Finally, Appendices A, B, C, and D provide details on the phase-map normalization, the derivation of the far-field diffractogram, the demonstration of its reality, and performing the inverse Fourier transform to arrive at g_z, respectively.

II. REVIEW OF NONLOCALITY EXPANSION: FAR-FIELD LIMIT

The purpose of this section is to provide a number of conceptual and technical cornerstones of the phase-contrast modality we are proposing. Briefly speaking, the emergence of intensity contrast from a phase-modulated (and *not* amplitude-modulated) wave field Ψ_0 in the transverse exit plane enjoys a

simple, local description in 2D Fourier space. The wave field Ψ_0 is induced by elastic interaction of an incoming plane wave (here assumed to be due to gravitational bending of its rays) with a sufficiently symmetric object. In the course of free-space propagation, self-interference generates intensity contrast analyzed by an observer far downstream of the exit plane. Though highly nonlinear in the phase variations, the extreme far-field situation assures that the 2D Fourier transform of this intensity contrast is local and thus contains direct information about the inducing phase map representing the projected object.

More specifically, when perfect spatial coherence of the incoming light can be assumed (which is the case in the setup of Fig. 1), Guigay's representation of I_z in the detector plane, emerging as a result of free-space propagation along a distance z of the pure-phase exit wave field $\Psi_0 = \sqrt{I_0}e^{i\phi(\mathbf{x}_\perp)}$ (no amplitude but only phase modulation in the transverse exit plane), applies if the observation of I_z is restricted to a small frequency band, centered at 3D wave number $k = \frac{2\pi}{\lambda}$. It is given as [14]

$$\mathcal{F}I_z = \int d^2x \Psi_0(\mathbf{x}_{\perp,-})\Psi_0^*(\mathbf{x}_{\perp,+})e^{-2\pi i\xi\cdot\mathbf{x}_\perp}, \tag{2}$$

where

$$\mathbf{x}_{\perp,\pm} \equiv \mathbf{x}_\perp \pm \frac{\pi z}{k}\xi,$$

and $\mathcal{F}$ denotes 2D Fourier transformation. Expanding the exponential in Eq. (2) and introducing the intensity contrast $g_z = \frac{I_z - I_0}{I_0}$, we obtain [11]

$$(\mathcal{F}g_z)(\xi) = (\mathcal{F}C)(\xi), \tag{3}$$

where the correlation function C is given as

$$C(\mathbf{x}_\perp,\xi) = \sum_{n=1}^{\infty}\sum_{l=0}^{n}\frac{(-i)^n}{n!}\binom{n}{l}(-1)^l\phi_-^l\phi_+^{n-l}, \tag{4}$$

where $\phi_\pm \equiv \phi(\mathbf{x}_{\perp,\pm})$. Whether the phase-overlap product $\phi_-\phi_+$ for a localized object is small, exhibiting spatial scales $a_1, a_2, \ldots$, is decided by the largest Fresnel number in $F_1 = \frac{a_1^2}{\lambda z}$, $F_2 = \frac{a_2^2}{\lambda z}$, … being smaller than the dimensionless frequency squared, $\sigma = \xi^2\pi\lambda z = (\xi_x^2 + \xi_y^2)\pi\lambda z$. Note that the symbol $\mathcal{F}$ on the right-hand side of Eq. (3) actually is a slight abuse of notation, since $C = C(\mathbf{x}_\perp,\xi)$ already depends on the conjugate wave-number vector ξ (pseudo Fourier transform). Expanding C in Eq. (4) in powers of $\phi_-\phi_+$, we may write

$$C(\mathbf{x}_\perp,\xi) = \sum_{l=0}^{\infty}(C_{l,\mathrm{cen}} + C_{l,\cos} + C_{l,\sin})$$

with the following definitions:

$$\begin{aligned}
C_{l,\mathrm{cen}} &= \frac{1}{(l!)^2}(\phi_-\phi_+)^l(1-\delta_{l0}),\\
C_{l,\cos} &= (\phi_-\phi_+)^l\sum_{k>l}^{\infty}\frac{(-1)^{k+l}}{(2k-l)!l!}(\phi_+^{2(k-l)} + \phi_-^{2(k-l)}),\\
C_{l,\sin} &= i(\phi_-\phi_+)^l\\
&\quad\times\sum_{k\geqslant l}^{\infty}\frac{(-1)^{k+l}}{(2k+1-l)!l!}(\phi_+^{2(k-l)+1} - \phi_-^{2(k-l)+1}).
\end{aligned} \tag{5}$$

Thus we arrive at

$$\mathcal{F}g_z = \sum_{l=0}^{\infty}\mathcal{F}g_{z,l} = \sum_{l=0}^{\infty}(\mathcal{F}C_{l,\mathrm{cen}} + \mathcal{F}C_{l,\cos} + \mathcal{F}C_{l,\sin}). \tag{6}$$

Here we refer to $g_{z,l}$ as the lth *onion shell* because it contains the layers of leading, subleading, etc. powers of ϕ_+. These arise by expanding the nth power of the binomial $\phi_+ - \phi_-$ appearing in the expansion of the exponential in Eq. (2) upon substitution of $\Psi_0 = \sqrt{I_0}e^{i\phi_-}$ and $\Psi_0^* = \sqrt{I_0}e^{-i\phi_+}$, compare with Eq. (4) (Pascal's triangle).

For the pseudo Fourier transforms appearing on the right-hand side of Eq. (6) we have explicitly (after shifting integration variables appropriately)

$$\begin{aligned}
\mathcal{F}C_{l,\mathrm{cen}} &= \frac{1}{(l!)^2}(1-\delta_{l0})\mathcal{F}(\phi_-\phi_+)^l,\\
\mathcal{F}C_{l,\cos} &= 2\mathcal{F}(\phi_-\phi_+)^l * \left[\cos(\sigma)\sum_{k>l}^{\infty}\frac{(-1)^{k+l}\mathcal{F}\phi^{2(k-l)}}{(2k-l)!l!}\right],\\
\mathcal{F}C_{l,\sin} &= 2\mathcal{F}(\phi_-\phi_+)^l * \left[\sin(\sigma)\sum_{k\geqslant l}^{\infty}\frac{(-1)^{k+l}\mathcal{F}\phi^{2(k-l)+1}}{(2k+1-l)!l!}\right],
\end{aligned}$$

where $*$ demands 2D convolution.

In the extreme far field the contribution $g_{z,l=0}$ in Eq. (6) dominates the entire diffractogram (with the exception of $\xi = 0$, see [11]). Considering that $\mathcal{F}C_{0,\mathrm{cen}} = 0$ and $(\phi_-\phi_+)^0 = 1$, the zeroth onion shell reads

$$\begin{aligned}
\mathcal{F}g_{z,0} &= 2\cos(\sigma)\sum_{k=1}^{\infty}\frac{(-1)^k\mathcal{F}\phi^{2k}}{(2k)!}\\
&\quad + 2\sin(\sigma)\sum_{k=0}^{\infty}\frac{(-1)^k\mathcal{F}\phi^{2k+1}}{(2k+1)!}.
\end{aligned} \tag{7}$$

The (good) approximation of the diffractogram, represented by Eq. (7), can be Fourier transformed to position space to gain back the intensity contrast $g_z(\mathbf{x}_\perp)$ in the far-field limit.

III. TOY MODEL FOR COLLISION OF PROJECTED OBJECTS WITHIN A BINARY

In this section we study the extreme far-field diffractogram and intensity contrast of a phase map meant to model the collision of projected objects within a binary, effectively giving rise to a phase map ϕ. As we have argued in Sec. II, the far-field situation is reached when the diffractogram becomes sufficiently local such that it is captured by the zeroth onion-shell approximation. On top of this, an additional simplification arises when all Fresnel numbers are sent to zero by effectively letting $z \to 0$ (*extreme far field*). In this case, the σ dependence of the diffractogram is universal: it exhibits rotational symmetry. In actual calculations we appeal to a Gaussian model for ϕ. This simplified version of admittedly more complex phase maps in realistic observational scenarios bears the advantage of being accessible to a largely analytical treatment.

A. Superposition of Gaussians in the phase map

Thus we study a phase map ϕ composed of two transversely separated Gaussian bumps of width $\sqrt{\omega}$ whose maxima are a

distance $|\mathbf{a}_\perp|$ apart. Such a phase map reads

$$\phi = S\left(e^{\frac{-(\mathbf{x}_\perp-\frac{\mathbf{a}_\perp}{2})^2}{2\omega}} + e^{\frac{-(\mathbf{x}_\perp+\frac{\mathbf{a}_\perp}{2})^2}{2\omega}}\right),$$

where $\mathbf{x}_\perp \equiv (x,y)^T$ and $\mathbf{a}_\perp \equiv (a_x,a_y)^T$. The two Gaussian bumps are chosen to be separated along the x axis without loss of generality. In the following, we write $a_x = a$. Therefore,

$$\phi = S\left[e^{\frac{-(x-\frac{a}{2})^2}{2\omega}} + e^{\frac{-(x+\frac{a}{2})^2}{2\omega}}\right]e^{-\frac{y^2}{2\omega}} \equiv \phi_{-a} + \phi_{+a}. \tag{8}$$

Since we wish to control the strength of phase variations in the phase map ϕ solely via the parameter S, we need to normalize ϕ/S to the interval [0,1] for all x, a, and ω.

B. Normalization of ϕ

It is useful to identify the following dimensionless variables in Eq. (8):

$$F = \frac{a}{\sqrt{\omega}}, \quad U = \frac{x}{\sqrt{\omega}}, \quad V = \frac{y}{\sqrt{\omega}}.$$

With these definitions Eq. (8) is recast as

$$\phi(U,V,F) = S\left[e^{-\frac{1}{2}(U-\frac{F}{2})^2} + e^{-\frac{1}{2}(U+\frac{F}{2})^2}\right]e^{-\frac{V^2}{2}}. \tag{9}$$

In Appendix A, the maxima ϕ/S are derived, depending on F in three domains.

$$\begin{aligned}
&\text{I} \;:\; F \in [0,2] :\; U_0 = 0,\\
&\text{II} \;:\; F \in [2,\approx 4] :\; U_{0_{2,3}} = \pm\left(W(F) + \frac{F}{2}\right),\\
&\text{III} :\; F \in [\approx 4,\infty] :\; U_{0_{2,3}} = \pm\frac{F}{2},
\end{aligned} \tag{10}$$

where $W(F)$ is defined in Eq. (A5) of Appendix A. Upon computing ϕ/S at U_0, one arrives at the normalized phase map $\hat{\phi}$ as

$$\hat{\phi}(U,V,F) = \frac{\phi(U,V,F)}{N(F)}. \tag{11}$$

The phase map $\hat{\phi}$ exhibits a maximum value S. For all F the function $N(F)$ in Eq. (11) is given as

$$N(F) = \frac{\phi(U_0,0,F)}{S} = \begin{cases} 2\,e^{-\frac{1}{2}(\frac{F}{2})^2}, & \text{I} \\ e^{-\frac{1}{2}(W(F)+F)^2} + e^{-\frac{1}{2}W(F)^2}, & \text{II} \\ 1 + e^{-\frac{F^2}{2}}, & \text{III}. \end{cases}$$

For small values of F, $W(F) \to -\frac{F}{2}$, implying $U_0 \to 0$. Thus $N(F)$ is a continuous function throughout regimes I,II. For large F, $W(F) \to 0$, as is easily seen from Eq. (A5). Therefore, $N(F)$ is continuous also throughout regimes II,III, see Fig. 2.

For notational simplicity we drop the hat symbol in what follows ($\hat{\phi} \to \phi$). As shown in Fig. 3, ϕ/S indeed is normalized to a maximum of unity.

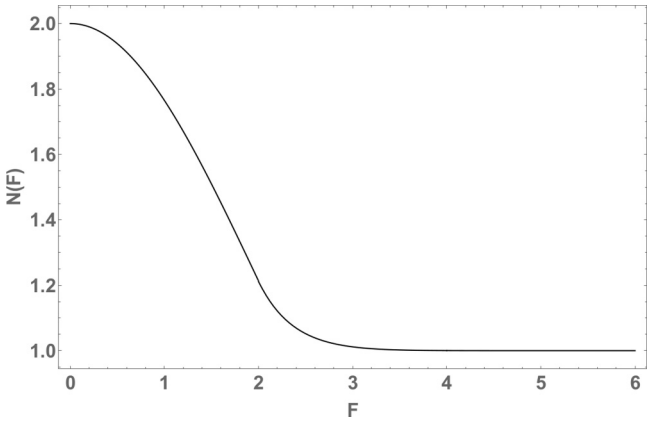

FIG. 2. Plot of $N(F)$ for all F [including regimes I,II,III defined in Eq. (10)]. Notice the smoothness of $N(F)$.

IV. FAR-FIELD INTENSITY CONTRAST

In Fourier space, the zeroth onion shell, computed from the phase map of Eq. (11), reads (see Appendix B for a derivation)

$$\begin{aligned}
\frac{\mathcal{F}g_{z,0}}{4\pi\omega} &= \cos(\sigma)\sum_{k=1}^{\infty}\frac{(-1)^k}{2k}\left(\frac{S}{N(F)}\right)^{2k} e^{\frac{-\sigma F_\omega}{2\pi(2k)}} \\
&\times \sum_{k'=0}^{2k}\frac{e^{-\frac{k'}{2}(1-\frac{k'}{2k})F^2}}{k'!(2k-k')!}e^{+\frac{i}{2}(1-\frac{2k'}{2k})\sqrt{\frac{\sigma_x F_a}{\pi}}} \\
&+ \sin(\sigma)\sum_{k=0}^{\infty}\frac{(-1)^k}{2k+1}\left(\frac{S}{N(F)}\right)^{2k+1} e^{\frac{-\sigma F_\omega}{2\pi(2k+1)}} \\
&\times \sum_{k'=0}^{2k+1}\frac{e^{-\frac{k'}{2}(1-\frac{k'}{2k+1})F^2}}{k'!(2k+1-k')!}e^{+\frac{i}{2}(1-\frac{2k'}{2k+1})\sqrt{\frac{\sigma_x F_a}{\pi}}},
\end{aligned} \tag{12}$$

where

$$F_\omega = \frac{\omega}{\lambda z}, \quad F_a = \frac{a^2}{\lambda z}, \quad F = \sqrt{\frac{F_a}{F_\omega}},$$
$$\sigma_x = \xi_x^2\pi\lambda z, \quad \sigma_y = \xi_y^2\pi\lambda z, \quad \sigma = \sigma_x + \sigma_y.$$

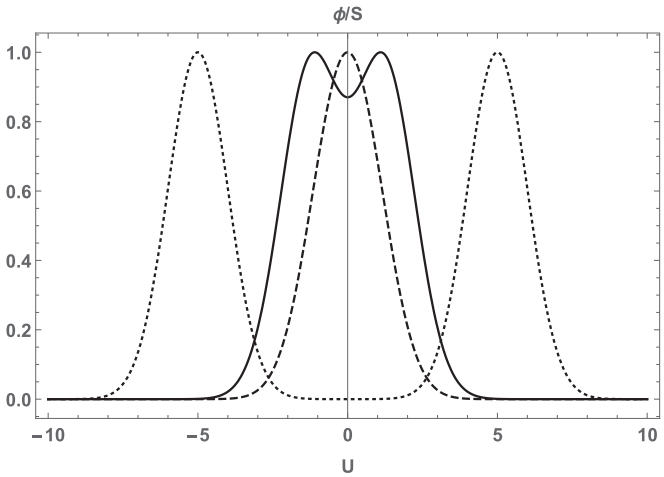

FIG. 3. Plot of normalized phase map ϕ/S for three different values of F: $F = 1$ (dashed), $F = 2.5$ (solid line), $F = 10$ (dotted).

Equation (12) is valid only for $F_a, F_\omega \ll 1$ (far-field limit), and one can show that the right-hand side is real (see Appendix C.).

The extreme far-field case of the zeroth onion shell is obtained from Eq. (12) by performing the limits $F_a \to 0$ and $F_\omega \to 0$ while simultaneously keeping the square root of their ratio $F = \sqrt{\frac{F_a}{F_\omega}}$ fixed and finite. This yields

$$\begin{aligned}\frac{\mathcal{F}g_{z,0}}{4\pi\omega} &= \cos(\sigma)\sum_{k=1}^{\infty}\frac{(-1)^k}{2k}\left(\frac{S}{N(F)}\right)^{2k}\\ &\times\sum_{k'=0}^{2k}\frac{e^{-\frac{k'}{2}(1-\frac{k'}{2k})F^2}}{k'!(2k-k')!}\\ &+\sin(\sigma)\sum_{k=0}^{\infty}\frac{(-1)^k}{2k+1}\left(\frac{S}{N(F)}\right)^{2k+1}\\ &\times\sum_{k'=0}^{2k+1}\frac{e^{-\frac{k'}{2}(1-\frac{k'}{2k+1})F^2}}{k'!(2k+1-k')!}.\end{aligned}\tag{13}$$

Motivated by Eq. (13) we introduce the scaling functions $S_1(S,F)$ and $S_2(S,F)$. They depend only on S and the ratio $F = \sqrt{\frac{F_a}{F_\omega}}$, which represents a measure of compactness of the binary. We have

$$\begin{aligned}S_1(S,F) &= \sum_{k=1}^{\infty}\frac{(-1)^k}{2k}\left(\frac{S}{N(F)}\right)^{2k}\sum_{k'=0}^{2k}\frac{e^{-\frac{k'}{2}(1-\frac{k'}{2k})F^2}}{k'!(2k-k')!},\\ S_2(S,F) &= \sum_{k=0}^{\infty}\frac{(-1)^k}{2k+1}\left(\frac{S}{N(F)}\right)^{2k+1}\sum_{k'=0}^{2k+1}\frac{e^{-\frac{k'}{2}(1-\frac{k'}{2k+1})F^2}}{k'!(2k+1-k')!},\end{aligned}\tag{14}$$

such that Eq. (13) is recast as

$$\frac{\mathcal{F}g_{z,0}}{4\pi\omega} = \cos(\sigma)S_1(S,F) + \sin(\sigma)S_2(S,F).\tag{15}$$

After transforming $\mathcal{F}g_{z,0}$ to position space, the intensity contrast $g_{z,0}$ of the zeroth onion shell is given in Eq. (D8) of Appendix D. In practice, the sums in Eq. (14) need to be truncated at $k_{\max}$. Evaluating $g_{z,0}$ for increasing values of S generally requires increasing values of $k_{\max}$. In Fig. 4 a plot of $g_{z,0}$ is shown.

In some observational situations only the much simpler expression for the *extreme* far field is needed. In this limit both F_a and F_ω are considered very small parameters, justifying that only their linear order is retained in expanding Eq. (D8) about $F_a = 0, F_\omega = 0$ (keeping $F \equiv \sqrt{\frac{F_a}{F_\omega}}$ finite). Equation (D8) then reduces to

$$\begin{aligned}g_{z,0} = \frac{F_\omega}{\pi}\Bigg[&\sin(\rho)\sum_{k=1}^{\infty}\frac{(-1)^k}{2k}\left(\frac{S}{N(F)}\right)^{2k}\sum_{k'=0}^{2k}\frac{e^{-\frac{k'}{2}(1-\frac{k'}{2k})F^2}}{k'!(2k-k')!}\\ &+\cos(\rho)\sum_{k=0}^{\infty}\frac{(-1)^k}{2k+1}\left(\frac{S}{N(F)}\right)^{2k+1}\\ &\times\sum_{k'=0}^{2k+1}\frac{e^{-\frac{k'}{2}(1-\frac{k'}{2k+1})F^2}}{k'!(2k+1-k')!}\Bigg],\end{aligned}\tag{16}$$

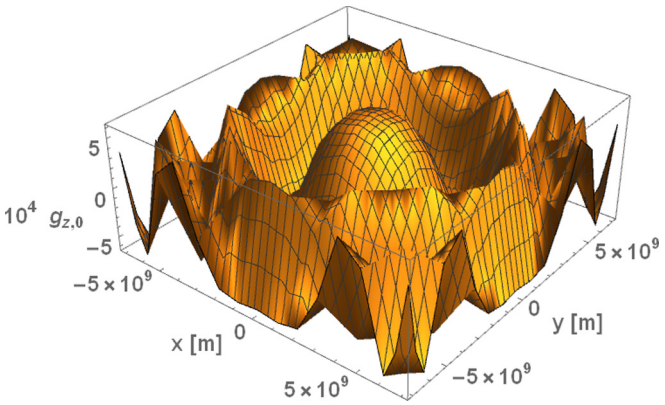

FIG. 4. 3D Plot of $g_{z,0}$ in Eq. (D8) for $S = 1$ and $\lambda z = 4.41 \times 10^{17}$ m^2, truncating the sum over k at $k_{\max} = 50$, which is reliable, see discussion in Sec. V. We have set $F = 10$, $F_\omega = 0.001$, $F_a = 0.1$, $a = 2.1 \times 10^7$ m. The corresponding phase map is represented in Fig. 3 (dotted line).

where

$$\rho \equiv \frac{x^2+y^2}{4\pi\lambda z}.$$

The same result is obtained by letting $F_a \to 0$ and $F_\omega \to 0$ in Eq. (12) and performing the inverse Fourier transformation subsequently. Notice that the expression on the right-hand side of Eq. (16) is cylindrically symmetric (it depends on x, y only via ρ). In terms of the scaling functions, defined in Eq. (14), Eq. (16) reads

$$\begin{aligned}g_{z,0} &= \frac{F_\omega}{\pi}[S_1\sin(\rho) + S_2\cos(\rho)]\\ &= \frac{F_\omega}{\pi}\sqrt{S_1^2+S_2^2}\sin\left(\rho+\arctan\frac{S_2}{S_1}\right).\end{aligned}\tag{17}$$

V. OBSERVABILITY OF THE INTENSITY CONTRAST

In the following example, we choose a binary with equal component masses and sizes (e.g., white dwarfs) to induce the diffraction of coherent background light when assumed to be modeled by the phase map of Eq. (11). Since the direct observation of SNe Ia progenitors is lacking [13], the characterization of such systems by virtue of their diffractive properties may be useful for the prediction of a particular nova and a potential standard candle assignment.

The typical diameter of a white dwarf is approximately $\sqrt{\omega} \approx 2 \times 10^7$ m [16]. To work with sufficiently small Fresnel numbers ($F_\omega < 0.001$ and $F_a \ll 1$), we demand $\lambda z \approx 4.4 \times 10^{17}$ m^2 [17]. This implies, e.g., $\lambda \approx 5 \times 10^{-7}$m (red light) $\Rightarrow z > 8.8 \times 10^{23}$m ≈ 0.3Mpc $\approx 9.3 \times 10^5$ ly or $\lambda \approx 0.3$ m (radio waves) $\Rightarrow z > 1.5 \times 10^{18}$m ≈ 48 pc ≈ 155 ly. How an effective value of F arises by projection of the binary orbit is depicted in Fig. 5 for a particular observational situation.

Let us assume that the period of orbit T_b of the binary is much larger than the time Δt required to cover a transverse distance

$$\Delta r = \Delta t v_t = \sqrt{x^2+y^2} = 2\pi\sqrt{\lambda z}.\tag{18}$$

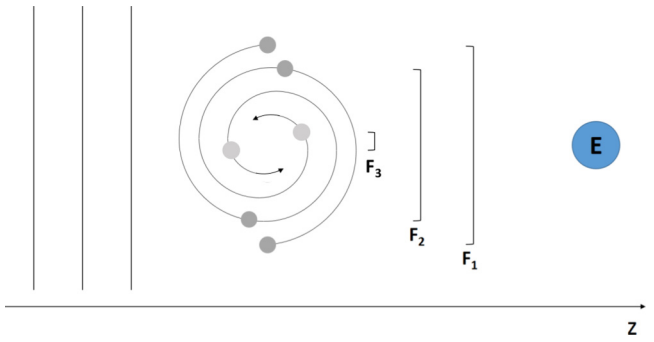

FIG. 5. Binary system with projected values of F for the particular case that the optical axis lies in the plane of orbit. E refers to a (terrestrial) observer. The more general situation of an inclined orbital plane is straightforward.

This expression for Δr follows from setting $\Delta\rho \equiv \rho_2 - \rho_1 = \pi$ to be able to sample one half of the spatial period of g_z, see Eq. (17) and Fig. 6. Then F can be considered a constant. Here v_t denotes the component of the relative velocity that is perpendicular to the optical axis between the center of mass of the binary and the observer. For example, if v_t is determined by the tangential velocity of earth's orbit, that is, $v_t = 2.6 \times 10^9$ m/d, and setting $\Delta r = 2 \times 10^9$ m (see Fig. 6), we obtain $\Delta t = 0.77$ d. Comparing this with a typical period of orbit in the range $T_b = 0.44 \ldots 3.22$ d [18], we conclude that much higher values of v_t are required. Assuming this to be the case, Eq. (18) can be solved for z as

$$z = \frac{1}{\lambda}\left(\frac{\Delta r}{2\pi}\right)^2. \tag{19}$$

Thus, the spatial structure I_z can be used to determine the distance to the binary. Moreover, a sufficiently dense spatial sampling of I_z, whose average then determines I_0, yields g_z, which, in turn, can be fitted to the expression in Eq. (17) to determine $\sqrt{\omega}$, S, and F. With $k_{\max} = 50$ summations defining

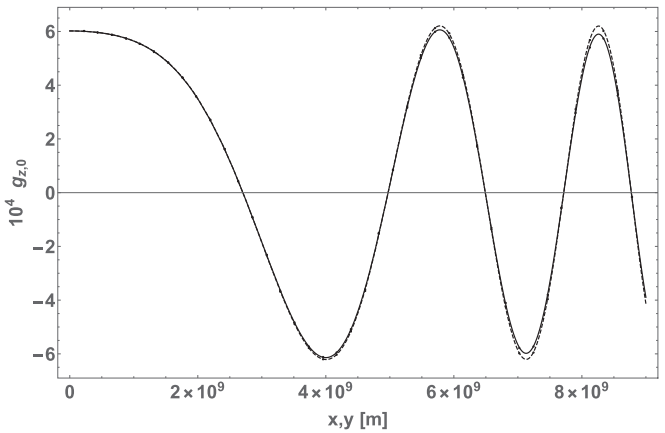

FIG. 6. Plot of $g_{z,0}(x, y = 0)$ (solid line) and $g_{z,0}(x = 0, y)$ (dashed line) according to Eq. (D8), demonstrating a slight asymmetry. Parameters are set as in Fig. 4. An increasing value of $S > 1$ only affects the normalization of g_z in a nonlinear way. On the other hand, an increasing value of F increases the asymmetry of $g_{z,0}(x, y = 0)$ vs $g_{z,0}(x = 0, y)$.

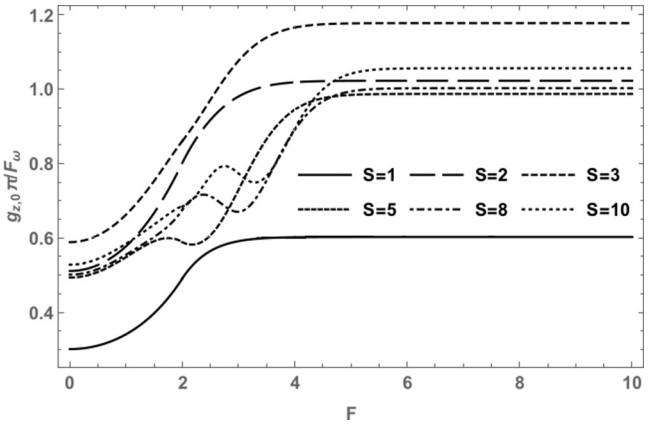

FIG. 7. Plot of $\frac{\pi}{F_\omega} g_{z,0}(\rho \to 0)$ in Eq. (16) as a function of $F \in [0,10]$ for $S = 1,2,3,5,8,10$. The sum defining the scaling function S_2 in Eq. (14) is truncated at $k_{\max} = 50$.

the scaling functions S_1 and S_2 in Eq. (17) [see Eq. (14)] converge to within machine precision for $0 \leqslant F \leqslant 10$ and $0 < S \leqslant 20$.

Alternatively, if $T_b \ll \Delta t = \frac{\Delta r}{v_t}$, then a temporal scan of g_z at, e.g., $x = y = 0 = \rho$, can be performed to examine the scaling behavior in S and F. That is, for each fixed value S there is a characteristic F dependence of g_z which is normalized in terms of F_ω. Observing $I_z(\rho = 0)$ at N equidistant times t_i $(i = 1, \ldots, N)$, the period T_b can be determined. Assuming that the plane of the binary's orbit contains the optical axis, the following dependence of F_i on t_i is substituted into Eq. (17):

$$F_i = F_0 \cos\left(2\pi \frac{t_i}{T_b} + \varphi\right), \tag{20}$$

where F_0 and the phase φ are fit parameters in addition to I_0, S, and F_ω.

We now discuss the characteristic F dependence of $g_z(\rho = 0)$. In Figs. 7 and 8 plots of $\frac{\pi}{F_\omega} g_{z,0}(\rho \to 0)$, as defined in Eq. (16), are depicted as functions of F for various values of S.

In analyzing these results, we refer to the F regimes as defined in Eq. (10). For regime I there is parabolic behavior; in

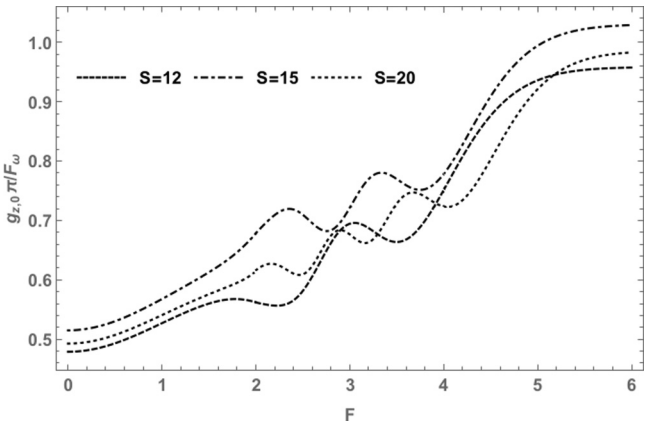

FIG. 8. Plot of $\frac{\pi}{F_\omega} g_{z,0}(\rho \to 0)$ in Eq. (16) as a function of $F \in [0,6]$ for $S = 12,15,20$. The sum defining the scaling function S_2 in Eq. (14) is truncated at $k_{\max} = 50$.

regime III all curves are constant for $F > 6$ (loss of correlation between the binary's components, see Fig. 7). Regime II exhibits genuine structure. Namely, for $S = 5$, $S = 8$ and $S = 10$ there are two local extrema. For larger values of S additional extrema develop within regime II (see Fig. 8). Therefore, counting extrema allows to identify useful priors for the fit of the S dependence.

VI. SUMMARY

In the present paper we have investigated the zeroth order of the nonlocality expansion [11] of intensity contrast in the free-space propagation of phase-modulated, perfectly spatiotemporally coherent wave fields when applied to an extreme far-field situation. In particular, we have assumed the inducing phase map to be a superposition of two equal-width Gaussians that are spatially separated. The motivation for this is the study of binary systems in astronomy that, due to their low luminosity, so far cannot be observed (e.g., white-dwarf binary as a progenitor of a SN Ia, neutron-star or black-hole binaries as progenitors to merger events which are accompanied by the emission of detectable gravitation waves). The idea is to exploit a coherent wave field, provided by a very distant and sufficiently luminous background source, whose phase is affected by transit through the binary via gravitational light bending. The more compact the binary's components, the better the approximation using Gaussian bumps in the effective phase map since the ratio between gravitational range and the extent of the mass distribution increases. In principle, the effective phase map emerges by analyzing the time delays along geodesics with associated deflection angles. This introduces quantitative differences compared to the assumed Gaussian shapes. Qualitatively, however, the use of Gaussian bumps is sufficient to point out the potential of our formalism. It is worth pointing out that radio observations are favored since in this case the far-field condition is easily satisfied for relatively small object-to-observer distances. In Sec. V we have discussed the example of a white-dwarf binary employing a wavelength of $\lambda = 0.3$ m. This is well contained, e.g., within the wavelength coverage of the square kilometer array (SKA).

Let us discuss two extreme modes of observation under the simplifying assumption that the binary's orbital plane contains the optical axis. (For an inclined plane, more fit parameters arise.) We have shown that a spatial scanning of the intensity (assuming a fast transverse, relative motion between observer and binary) allows the extraction of the distance to the binary in a controlled and simple way if the frequency bandwidth of observation is not too large. Moreover, spatial scanning allows fitting the unmodulated intensity I_0, the two Fresnel numbers relating to the components' size and separation, and the diffractive power of the overall system. Intensity contrast is small (typically 10^{-4} or lower), and the question arises whether the observational signal-to-noise ratio (Poisson noise of detectors can be reduced by increased exposure times and/or spectral bandwidths) allows the measurement of such small intensity variations. Alternatively, if transverse, relative motion is slow, a temporal scan reveals the binary's orbital period and can also be used to fit I_0, the two Fresnel numbers, and, in particular, the overall diffractive power. A direct extraction of the distance to the binary is impossible in this mode. Often the observational situation will be a mix of these two cases, and more sophisticated strategies of data analysis are in order.

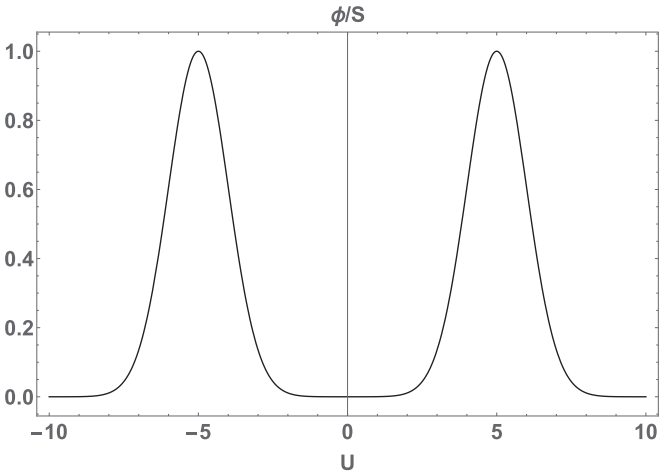

FIG. 9. The case $F = 10$. The Gaussian bumps in ϕ/S are separated along the U axis, and their two (degenerate) maxima practically do not exceed unity.

To the best of the authors' knowledge, the modality of propagation-based phase contrast has not yet been applied to astronomical observation. If realizable, then a bimodal strategy (gravitational waves and propagation-based phase contrast) of observing in spirals appears possible to detect and analyze the binary *well before* the merger occurs, given the existence of a distant, luminous, and ergodic background light source.

ACKNOWLEDGMENT

We would like to thank Bjoern Matthias for his helpful comments on the manuscript.

APPENDIX A: DERIVATION OF PHASE NORMALIZATION FACTOR $N(F)$

Plotting ϕ/S of Eq. (9) for selected values of F indicates the problem in normalizing the phase map to a maximum value of unity (see Figs. 9, 10, and 11).

To control the diffractive power, as imprinted into the phase map, solely via S, we need to normalize ϕ/S in terms of $N(F)$ such that for an arbitrary value of F the maximum of $\frac{\phi}{N(F)S}$ always is unity:

$$\forall F \in \mathbb{R} \max \frac{\phi(U,V,F)}{N(F)S} = 1. \tag{A1}$$

To find the extrema of ϕ/S we analyze the conditions $\frac{\partial\phi}{\partial U} = 0$ and $\frac{\partial\phi}{\partial V} = 0$. Straightforward calculation yields

$$V = 0\,,$$
$$\tanh\left(\frac{UF}{2}\right) = \pm\frac{2U}{F}. \tag{A2}$$

The transcendental equation, Eq. (A2), which is reminiscent of the equation satisfied by the magnetization in the mean-field treatment of the 1D Ising model [19], requires a closer

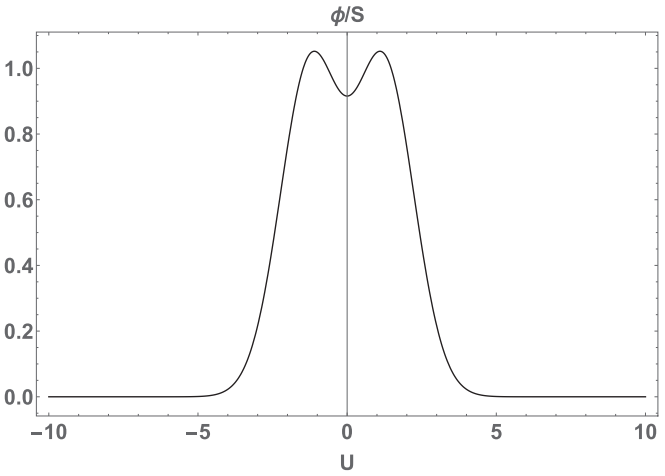

FIG. 10. The case $F = 2.5$. The Gaussian bumps overlap one another so the two (degenerate) maxima now exceed unity.

examination. For various values of F, we numerically obtain the following roots U_0 of Eq. (A2):

Since $\lim_{x\to\infty} \tanh x = 1$, large values of F imply that the approach $U_{0_{2,3}} \to \pm F/2$ is exponentially fast. On the other hand, for $F \to 0$ we have $U_0 = 0$. As one can easily argue by expanding the left-hand side of (A2) about zero and by appealing to the convexity of $U(F)$, there is critical behavior at $F_c = 2$, as indicated in Fig. 12.

To analyze the transition indicated in Fig. 12 by the solid line, we require an approximate solution to Eq. (A2). Table I suggests to expand the hyperbolic tangent in powers of $W \equiv (U - \frac{F}{2})$. Up to quadratic order this yields

$$\tanh\left(\frac{UF}{2}\right) \approx \tanh\left(\frac{F^2}{4}\right) + \frac{1}{\cosh^2\left(\frac{F^2}{4}\right)}\frac{F}{2}\left(U - \frac{F}{2}\right) - \frac{\tanh\left(\frac{F^2}{4}\right)}{\cosh^2\left(\frac{F^2}{4}\right)}\frac{F^2}{4}\left(U - \frac{F}{2}\right)^2. \tag{A3}$$

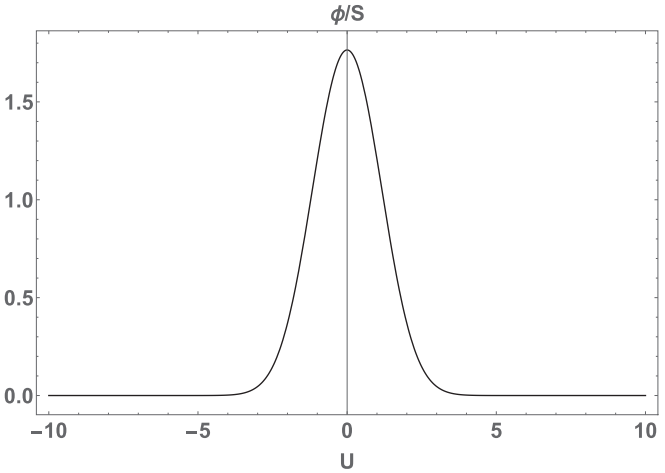

FIG. 11. The case $F = 1$. The two Gaussian bumps now overlap substantially such that a single, global maximum arises at $U = 0$.

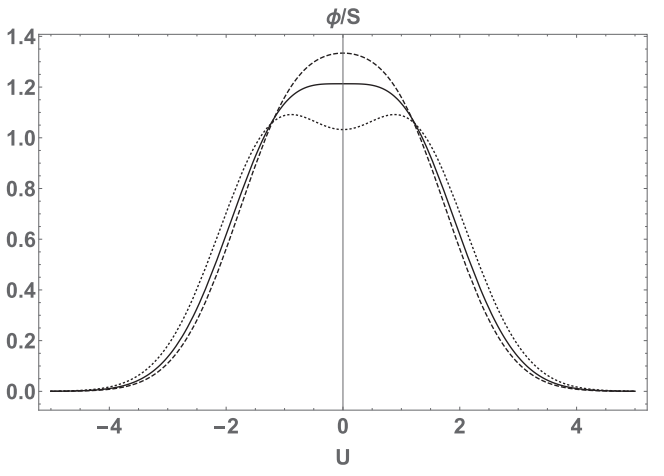

FIG. 12. Plot of ϕ/S for $F = 2.3$ (dotted), $F = F_c = 2.0$ (solid line), $F = 1.8$ (dashed), $S = 1$. With smaller F, the two Gaussian bumps overlap such that their shared, local minimum at $U = 0$ (dotted) switches to a global maximum (dashed).

Introducing the following abbreviations in Eq. (A3),

$$C_0(F) = \tanh\left(\frac{F^2}{4}\right),$$
$$C_1(F) = \frac{1}{\cosh^2\left(\frac{F^2}{4}\right)},$$
$$C_2(F) = \frac{\tanh\left(\frac{F^2}{4}\right)}{\cosh^2\left(\frac{F^2}{4}\right)},$$

Eq. (A2) approximates as

$$C_0(F) + \frac{F}{2}C_1(F)W - \frac{F^2}{4}C_2(F)W^2 = \frac{2}{F}\left(W + \frac{F}{2}\right). \tag{A4}$$

Solving Eq. (A4) for W, we arrive at

$$W(F) = \left(\frac{2}{C_2(F)F^2}\right)\left[-\left(\frac{2}{F} - \frac{F}{2}C_1(F)\right) + \sqrt{\left(\frac{2}{F} - \frac{F}{2}C_1(F)\right)^2 - C_2(F)F^2[1 - C_0(F)]}\right]. \tag{A5}$$

TABLE I. Values of F and related extrema U_0.

Values of F	Extrema U_0
$F = 1$	$U_0 = 0$
$F = 2$	$U_0 = 0$
$F = 3$	$U_{0_1} = 0$
	$U_{0_{2,3}} = \pm 1.463$
$F = 4$	$U_{0_1} = 0$
	$U_{0_{2,3}} = \pm 1.999$
$F = 6$	$U_{0_1} = 0$
	$U_{0_{2,3}} = \pm 3$
$F = 10$	$U_{0_1} = 0$
	$U_{0_{2,3}} = \pm 5$

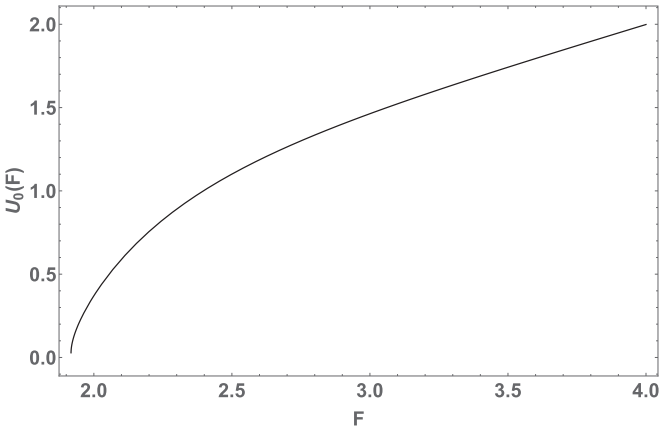

FIG. 13. Plot of $U_0(F) = +[W(F) + \frac{F}{2}]$, illustrating the locations of maxima U_0 in dependence on F as predicted by the approximate solution (A5) of Eq. (A2) for $1.9 \leqslant F \leqslant 4$.

Notice that the alternative solution, replacing the plus sign by a minus sign in front of the square root in Eq. (A5), would violate the smallness assumption on W, and therefore needs to be discarded. Accordingly, the locations of the maxima are approximately given by $U_0(F) = \pm[W(F) + \frac{F}{2}]$, exploiting the $\mathbf{Z}_2$ symmetry of ϕ. This is depicted in Fig. 13.

APPENDIX B: DERIVATION OF $\mathcal{F}g_{z,0}$ OF EQ. (12)

We note that Eq. (7) involves the Fourier transform of the nth power of the phase map $\mathcal{F}\phi^n$. We calculate

$$\phi^n = (\phi_{-a} + \phi_{+a})^n = \sum_{k'=0}^{n} \binom{n}{k'} \phi_{-a}^{k'} \phi_{+a}^{n-k'} ,$$

in which

$$\phi_{-a}^{k'} = \left(\frac{S}{N(F)}\right)^{k'} e^{-(x-\frac{a}{2})^2 \frac{k'}{2\omega}} e^{-\frac{y^2 k'}{2\omega}},$$

$$\phi_{+a}^{n-k'} = \left(\frac{S}{N(F)}\right)^{n-k'} e^{-(x+\frac{a}{2})^2 \frac{n-k'}{2\omega}} e^{-\frac{y^2(n-k')}{2\omega}} .$$

Pieced together, we have

$$\phi^n = \left(\frac{S}{N(F)}\right)^n e^{-\frac{ny^2}{2\omega}} \sum_{k'=0}^{n} \frac{n!}{k'!(n-k')!} \times e^{-\left[(x-\frac{a}{2})^2 \frac{k'}{2\omega} + (x+\frac{a}{2})^2 \frac{n-k'}{2\omega}\right]}. \quad \text{(B1)}$$

The exponent in Eq. (B1) simplifies to

$$\left(x - \frac{a}{2}\right)^2 \frac{k'}{2\omega} + \left(x + \frac{a}{2}\right)^2 \frac{n-k'}{2\omega} = [n(x + \tfrac{a}{2})^2 - 2k'ax] \frac{1}{2\omega}.$$

Applying the Fourier transform to ϕ^n,

$$(\mathcal{F}\phi^n) = \int_{-\infty}^{\infty} \int_{-\infty}^{\infty} \phi^n e^{-i\xi_x x} e^{-i\xi_y y}\, dx dy , \quad \text{(B2)}$$

we obtain

$$(\mathcal{F}\phi^n) = \sum_{k'=0}^{n} \frac{n!}{k'!(n-k')!} \left(\frac{S}{N(F)}\right)^n \int_{-\infty}^{\infty} e^{-\frac{ny^2}{2\omega}} e^{-i\xi_y y} dy \times \int_{-\infty}^{\infty} e^{-[n(x+\frac{a}{2})^2 - 2k'ax]\frac{1}{2\omega}} e^{-i\xi_x x}\, dx .$$

In order to solve the integrals, we must complete the square in each exponent. The y integral reads

$$\int_{-\infty}^{\infty} e^{-\left(\sqrt{\frac{ny^2}{2\omega}} + i\xi_y \sqrt{\frac{\omega}{2n}}\right)^2} e^{-\xi_y^2 \frac{\omega}{2n}} dy .$$

Rearranging factors and multiplying by unity, this integral can be performed as

$$\sqrt{\frac{2\omega}{n}} e^{-\xi_y^2 \frac{\omega}{2n}} \underbrace{\int_{-\infty}^{\infty} e^{-\frac{n}{2\omega}(y + \xi_y \frac{i\omega}{n})^2} \sqrt{\frac{n}{2\omega}} dy}_{\sqrt{\pi}} = \sqrt{\frac{2\pi\omega}{n}} e^{-\xi_y^2 \frac{\omega}{2n}} . \quad \text{(B3)}$$

The next step is to evaluate the x integral. In analogy to the y integration, we obtain

$$\sqrt{\frac{2\omega}{n}} e^{-\frac{n}{2\omega}\left[\frac{a_x^2}{4} - (\frac{i\xi_x\omega}{n} + \frac{a_x}{2} - \frac{a_x k'}{n})^2\right]} \times \underbrace{\int_{-\infty}^{\infty} e^{-\frac{n}{2\omega}\left[\left(x + (\frac{i\xi_x\omega}{n} + \frac{a_x}{2} - \frac{a_x k'}{2})\right)^2\right]} \sqrt{\frac{n}{2\omega}} dx}_{\sqrt{\pi}} . \quad \text{(B4)}$$

Referring to Eqs. (B3) and (B4), Eq. (B2) becomes

$$(\mathcal{F}\phi^n) = \left(\frac{S}{N(F)}\right)^n \frac{2\pi\omega}{n} e^{-\xi_y^2 \frac{\omega}{2n}} \sum_{k'=0}^{n} \frac{n!}{k'!(n-k')!} \times e^{-\frac{n}{2\omega}[\frac{a_x^2}{4} - (\frac{i\xi_x\omega}{n} + \frac{a_x}{2} - \frac{a_x k'}{n})^2]}. \quad \text{(B5)}$$

In Eq. (B5), we may introduce the dimensionless variables

$$F_\omega = \frac{\omega}{\lambda z}, \quad F_a = \frac{a_\perp^2}{\lambda z}, \quad F = \sqrt{\frac{F_a}{F_\omega}},$$
$$\sigma_x = \xi_x^2 \pi \lambda z, \quad \sigma_y = \xi_y^2 \pi \lambda z, \quad \sigma = \sigma_x + \sigma_y, \quad \text{(B6)}$$

where F_ω, F_a are Fresnel numbers with respect to ω, a. While $F_\omega, F_a > 1$ correspond to the near-field case, the opposite situation $F_\omega, F_a \ll 1$ characterizes the far field.

Inserting Eqs. (B6) and Eq. (B5) into Eq. (7) and distinguishing the cases $n = 2k$ and $n = 2k+1$ ($k = 0,1,2,\ldots$), we arrive at Eq. (12).

TABLE II. Pairing of terms in the cosine term under the sum over k' in Eq. (12). Here M is an integer running from $M = 0$ to $M = k - 1$. The central term $k' = k$ is real by itself and represented by the last line.

k'	$\frac{1}{k'!(2k-k')!}$	$-\frac{k'}{2}(1-\frac{k'}{2k})F^2$	$+\frac{i}{2}(1-\frac{2k'}{2k})\sqrt{\frac{\sigma_x F_a}{\pi}}$
M	$\frac{1}{M!(2k-M)!}$	$-\frac{M}{2}(1-\frac{M}{2k})F^2$	$+\frac{i}{2}(1-\frac{M}{k})\sqrt{\frac{\sigma_x F_a}{\pi}}$
$2k-M$	$\frac{1}{M!(2k-M)!}$	$-\frac{M}{2}(1-\frac{M}{2k})F^2$	$-\frac{i}{2}(1-\frac{M}{k})\sqrt{\frac{\sigma_x F_a}{\pi}}$
$k' = k$	$\frac{1}{(k!)^2}$	$-\frac{k}{4}F^2$	0

APPENDIX C: PROOF OF REALITY OF RIGHT-HAND SIDE OF EQ. (12)

The factors $e^{+\frac{i}{2}(1-\frac{2k'}{2k})\sqrt{\frac{\sigma_x F_a}{\pi}}}$ and $e^{+\frac{i}{2}(1-\frac{2k'}{2k+1})\sqrt{\frac{\sigma_x F_a}{\pi}}}$ of Eq. (12) are complex and thus of magnitude unity. Let us now evaluate the sum over k' in order to check if the imaginary part of the expression vanishes.

Table II shows that there are pairings whose coefficients are identical and for which the exponents are complex conjugates of one another. The center term in the sum $\sum_{k'=0}^{2k} \ldots$ at $k'=k$ has no partner and is real by itself.

Treating the sin term in Eq. (12) analogously in identifying $2k \to 2k+1$ reveals similar pairings. The only difference under the sum $\sum_{k'=0}^{2k+1}$ is the absence of the center term because there is an even number of summands. This proves that the expression on the right-hand side Eq. (12) is real and can be recast as

$$\frac{\mathcal{F}g_{z,0}}{8\pi\omega} = \cos(\sigma)\sum_{k=1}^{\infty}\frac{(-1)^k}{2k}\left(\frac{S}{N(F)}\right)^{2k} e^{\frac{-\sigma F_\omega}{2\pi(2k)}}\left\{\sum_{k'=0}^{k-1}\frac{e^{-\frac{k'}{2}(1-\frac{k'}{2k})F^2}}{k'!(2k-k')!}\cos\left[\frac{1}{2}\left(1-\frac{2k'}{2k}\right)\sqrt{\frac{\sigma_x F_a}{\pi}}\right] + \overbrace{\frac{1}{2}\frac{1}{(k!)^2}e^{-\frac{k}{4}F^2}}^{\text{centerterm}}\right\}$$
$$\times\ \sin(\sigma)\sum_{k=0}^{\infty}\frac{(-1)^k}{2k+1}\left(\frac{S}{N(F)}\right)^{2k+1} e^{\frac{-\sigma F_\omega}{2\pi(2k+1)}}\sum_{k'=0}^{k}\frac{e^{-\frac{k'}{2}(1-\frac{k'}{2k+1})F^2}}{k'!(2k+1-k')!}\cos\left[\frac{1}{2}\left(1-\frac{2k'}{2k+1}\right)\sqrt{\frac{\sigma_x F_a}{\pi}}\right].$$

APPENDIX D: TRANSFORMATION OF $\mathcal{F}g_{z,0}$ TO POSITION SPACE

The inverse Fourier transformation is defined as

$$g_{z,0} = \frac{1}{(2\pi)^2}\int_{-\infty}^{\infty}\int_{-\infty}^{\infty}(\mathcal{F}g_{z,0})e^{-i\xi_x x}e^{-i\xi_y y}\,d\xi_x d\xi_y.$$

Performing the inverse Fourier transform of the expression in Eq. (12) using

$$2\cos(\sigma) = \underbrace{e^{i\sigma}}_{\text{1st cos-term}} + \underbrace{e^{-i\sigma}}_{\text{2nd cos-term}} \tag{D1}$$

and

$$2i\sin(\sigma) = \underbrace{e^{i\sigma}}_{\text{1st sin-term}} - \underbrace{e^{-i\sigma}}_{\text{2nd sin-term}} \tag{D2}$$

leads to

$$g_{z,0} = \frac{2\pi\omega}{(2\pi)^2}\sum_{k=1}^{\infty}\frac{(-1)^k}{2k}\left(\frac{S}{N(F)}\right)^{2k}\sum_{k'=0}^{2k}\frac{e^{-\frac{k'}{2}(1-\frac{k'}{2k})F^2}}{k'!(2k-k')!}$$
$$\times\left[\underbrace{\iint e^{i(\xi_x^2+\xi_y^2)\pi\lambda z}e^{-\frac{(\xi_x^2+\xi_y^2)\omega}{2(2k)}}e^{+\frac{i}{2}(1-\frac{2k'}{2k})\xi_x a}e^{-i(\xi_x x+\xi_y y)}d\xi_x d\xi_y}_{\text{induced by 1st cos-term}} + \underbrace{\iint e^{-i(\xi_x^2+\xi_y^2)\pi\lambda z}e^{-\frac{(\xi_x^2+\xi_y^2)\omega}{2(2k)}}e^{+\frac{i}{2}(1-\frac{2k'}{2k})\xi_x a}e^{-i(\xi_x x+\xi_y y)}d\xi_x d\xi_y}_{\text{induced by 2nd cos-term}}\right]$$
$$+\frac{2\pi\omega}{(2\pi)^2}\sum_{k=0}^{\infty}\frac{(-1)^k}{2k+1}\left(\frac{S}{N(F)}\right)^{2k+1}\sum_{k'=0}^{2k+1}\frac{e^{-\frac{k'}{2}(1-\frac{k'}{2k+1})F^2}}{k'!(2k+1-k')!}\frac{1}{i}$$
$$\times\left[\underbrace{\iint e^{i(\xi_x^2+\xi_y^2)\pi\lambda z}e^{-\frac{(\xi_x^2+\xi_y^2)\omega}{2(2k+1)}}e^{+\frac{i}{2}(1-\frac{2k'}{2k+1})\xi_x a}e^{-i(\xi_x x+\xi_y y)}d\xi_x d\xi_y}_{\text{induced by 1st sin-term}} - \underbrace{\iint e^{-i(\xi_x^2+\xi_y^2)\pi\lambda z}e^{-\frac{(\xi_x^2+\xi_y^2)\omega}{2(2k+1)}}e^{+\frac{i}{2}(1-\frac{2k'}{2k+1})\xi_x a}e^{-i(\xi_x x+\xi_y y)}d\xi_x d\xi_y}_{\text{induced by 2nd sin-term}}\right]. \tag{D3}$$

Certain correspondences between these four integrals can be exploited. In Eq. (D3) the only integral which needs to be solved explicitly is, e.g., the one induced by the first cos term. Let us therefore consider

$$\int_{-\infty}^{\infty}d\xi_x e^{i\xi_x^2\pi\lambda z}e^{-\frac{\xi_x^2\omega}{2(2k)}}e^{+\frac{i}{2}(1-\frac{2k'}{2k})\xi_x a}e^{-i\xi_x x}\int_{-\infty}^{\infty}d\xi_y e^{i\xi_y^2\pi\lambda z}e^{-\frac{\xi_y^2\omega}{2(2k)}}e^{-i\xi_y y}. \tag{D4}$$

First, we complete the square in the exponent of the first line, given as

$$\left\{\xi_x^2\left(i\pi\lambda z - \frac{\omega}{2(2k)}\right) + \xi_x\left[\frac{i}{2}\left(1-\frac{k'}{k}\right)a - ix\right]\right\},$$

to arrive at

$$\left(i\pi\lambda z-\frac{\omega}{2(2k)}\right)\left(\overbrace{\xi_x-\left(\frac{\frac{-i}{4}\left(1-\frac{k'}{k}\right)a}{i\pi\lambda z-\frac{\omega}{2(2k)}}+\frac{ix}{2\left(i\pi\lambda z-\frac{\omega}{2(2k)}\right)}\right)}^{\xi_x'}\right)^2-\left(\frac{\frac{-i}{4}\left(1-\frac{k'}{k}\right)a}{\sqrt{i\pi\lambda z-\frac{\omega}{2(2k)}}}+\frac{ix}{2\sqrt{i\pi\lambda z-\frac{\omega}{2(2k)}}}\right)^2. \tag{D5}$$

In performing the Gaussian ξ_x integration, based on the exponent in Eq. (D5), we have

$$\frac{\sqrt{\pi}}{\sqrt{\frac{\omega}{2(2k)}-i\pi\lambda z}}e^{-\left(\frac{\frac{-i}{4}\left(1-\frac{k'}{k}\right)a}{\sqrt{i\pi\lambda z-\frac{\omega}{2(2k)}}}+\frac{ix}{2\sqrt{i\pi\lambda z-\frac{\omega}{2(2k)}}}\right)^2}.$$

The remaining ξ_y integral in Eq. (D4), subject to the integrand

$$\exp\left[\xi_y^2\left(i\pi\lambda z-\frac{\omega}{2(2k)}\right)-i\xi_y y\right],$$

can be performed in close analogy. One obtains

$$\frac{\sqrt{\pi}}{\sqrt{\frac{\omega}{2(2k)}-i\pi\lambda z}}e^{\frac{y}{2\sqrt{i\pi\lambda z-\frac{\omega}{2(2k)}}}}.$$

Having the integral associated with the first cos term at our disposal, the remaining three terms in Eq. (D3) can then be deduced as follows. The term induced by the second cos term can be obtained from the one induced by the first cos term in letting $\lambda\to-\lambda$. To obtain the integrals induced by the two sin terms, we have to perform the following substitutions in the integrals. For the integral associated with the first cos term we modify

$$2k\to 2k+1 \quad\text{and}\quad \text{factor1}\to\text{factor}\frac{1}{i} \tag{D6}$$

to obtain the integral associated with the first sin term. Accordingly, we modify

$$2k\to 2k+1 \quad\text{and}\quad \text{factor1}\to\text{factor}i \tag{D7}$$

to map the integral associated with the second cos term to the one associated with the second sin term. Piecing everything together, we finally arrive at the exact expression for the intensity contrast in position space,

$$\begin{aligned}g_{z,0}=&\frac{F_\omega}{2\pi}\sum_{k=1}^{\infty}\frac{(-1)^k}{2k}\left(\frac{S}{N(F)}\right)^{2k}\sum_{k'=0}^{2k}\frac{e^{-\frac{k'}{2}\left(1-\frac{k'}{2k}\right)F^2}}{k'!(2k-k')!}\left[\frac{\pi e^{-i\frac{\left[F_a(k'-k)^2+2F_a(2k)\frac{x}{a}(k-k')+(2k)^2\left(\frac{x^2+y^2}{\lambda z}\right)\right]}{2(2k)[2\pi(2k)+iF_\omega]}}}{\left(\frac{F_\omega}{2(2k)}-i\pi\right)}+\text{c.c.}\right]\\&+\frac{F_\omega}{2\pi i}\sum_{k=0}^{\infty}\frac{(-1)^k}{2k+1}\left(\frac{S}{N(F)}\right)^{2k+1}\sum_{k'=0}^{2k+1}\frac{e^{-\frac{k'}{2}\left(1-\frac{k'}{2k+1}\right)F^2}}{k'!(2k+1-k')!}\left[\frac{\pi e^{-i\frac{\left[F_a(2k+1-2k')^2+4F_a(2k+1)\frac{x}{a}(2k+1-2k')+4(2k+1)^2\left(\frac{x^2+y^2}{\lambda z}\right)\right]}{8(2k+1)[2\pi(2k+1)+iF_\omega]}}}{\left(\frac{F_\omega}{2(2k+1)}-i\pi\right)}-\text{c.c.}\right],\end{aligned} \tag{D8}$$

where c.c. stands for the complex conjugate of the preceding term. Therefore, $g_{z,0}$ is real, as it must be, since no cancellation of imaginary parts may occur in between different onion-shell expansion terms.

[1] D. Paganin, *Coherent X-ray Optics* (Oxford University Press, Oxford, England, 2006).

[2] A. Snigirev, I. Snigireva, V. Kohn, S. Kuznetsov, and I. Schelokov, Rev. Sci. Instrum. **66**, 5486 (1995).

[3] S. W. Wilkins, T. E. Gureyev, D. Gao, A. Pogany, and A. W. Stevenson, Nature (London) **384**, 335 (1996).

[4] P. Cloetens, R. Barrett, J. Baruchel, J.-P. Guigay, and M. Schlenker, J. Phys. D **29**, 133 (1996).

[5] P. Cloetens, Ph.D. Thesis, Vrije Universiteit Brussel, 1999.

[6] K. A. Nugent, T. E. Gureyev, D. F. Cookson, D. Paganin, and Z. Barnea, Phys. Rev. Lett. **77**, 2961 (1996).

[7] T. E. Gureyev, A. Pogany, D. M. Paganin, and S. W. Wilkins, Opt. Commun. **231**, 53 (2004).

[8] T. E. Gureyev, Ya. I. Nesterets, D. M. Paganin, A. Pogany, and S. W. Wilkins, Opt. Commun. **259**, 569 (2006).

[9] J. Moosmann, A. Ershov, V. Altapova, T. Baumbach, M. S. Prasad, C. LaBonne, X. Xiao, J. Kashef, and R. Hofmann, Nature (London) **497**, 374 (2013).

[10] M. Born and E. Wolf, *Principles of Optics*, 7th ed. (Cambridge University Press, Cambridge, England, 1999).
[11] S. Hahn, Y. Müller, R. Hofmann, J. Moosmann, O. Öktem, L. Helfen, J.-P. Guigay, Th. van de Kamp, and T. Baumbach, Phys. Rev. A **93**, 053834 (2016).
[12] B. P. Abbott *et al.*, Phys. Rev. Lett. **119**, 161101 (2017).
[13] B. Dilday *et al.*, Science **337**, 942 (2012).
[14] J.-P. Guigay, Optik **49**, 121 (1977).
[15] F. Trost, S. Hahn, Y. Müller, S. Gasilov, R. Hofmann, and T. Baumbach, Sci. Rep. **7**, 17706 (2017).
[16] S. Chandrasekhar, Mon. Not. R. Astron. Soc. **95**, 207 (1935).
[17] In case of cosmological distances the use of $\widehat{\lambda z} \equiv \lambda_{\rm em} \int_0^\zeta d\zeta' \frac{\zeta'+1}{H(\zeta')}$ instead of λz in the definition of F_ω and F_a is mandatory, where $\lambda_{\rm em}$ denotes the wavelength at emission, ζ is cosmological redshift, and $H(\zeta)$ represents the cosmological model for the Hubble parameter.
[18] G. Nelemans, R. Napiwotzki, C. Karl, T. R. Marsh, B. Voss, G. Roelofs, R. G. Izzard, M. Montgomery, T. Reerink, N. Christlieb, and D. Reimers, Astron. Astrophys. **440**, 1087 (2005).
[19] F. Reif, *Statistical Physics*, Berkeley Physics Course Vol. 5 (McGraw-Hill, New York, 1965).